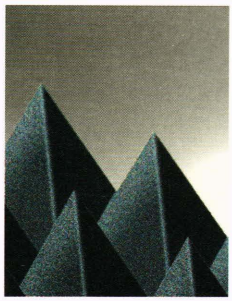

Ultraviolet and Visible Imager Simulation

Steve M. Yionoulis

The performance of spaceborne instruments designed to obtain images in the ultraviolet and visible spectra (110- to 900-nm wavelengths) was simulated to assist in mission planning for the Midcourse Space Experiment. Among the effects modeled were targets of various shapes; plumes; sensor effects; and spacecraft effects such as motion (streaking) and backgrounds, including stars, zodiacal light, dayglow, and Rayleigh scattering.

INTRODUCTION

The Applied Physics Laboratory performed spacecraft development and integration for the Midcourse Space Experiment (MSX), a DoD-sponsored near-Earth spacecraft mission to be launched in 1995. One of the satellite subsystems contains the Ultraviolet and Visible Imagers and Spectrographic Imagers (UVISI) instruments (four imagers and five imaging spectrographs). The imagers include both narrow and wide field-of-view (NFOV and WFOV) sensors for various segments of the ultraviolet and visible spectra. Table 1 lists characteristics of each of the imagers.

The UVISI instrumentation was designed to perform in-orbit, closed-loop tracking of various objects such as spacecraft, ground-launched rockets, stars, auroral surges, and clouds. Early in the MSX program, APL recognized that a simulation of the images generated by the UVISI instruments could play an important role in this and future satellite missions. As a result, APL developed a software program to perform the simulation.

The performance of both the spectrographs and the imagers was simulated using the APL-developed program;[1,2] however, only the four ultraviolet and visible imagers are discussed in this article. The objectives of the simulation were to

1. Analyze instrument performance against reasonable backgrounds
2. Provide sequences of images for the UVISI image processor for testing target identification algorithms
3. Provide a tool for mission simulation, planning, and analysis

For the MSX program, the simulation proved to be a valuable tool. It was used to determine when and under what conditions certain objects are visible for the purposes of (1) designing and analyzing a closed-loop tracking system, (2) testing instrument automatic gain control (AGC) algorithms, and (3) evaluating the effectiveness of each of the imagers and spectrographic instruments.[3-6]

Table 1. UVISI imager characteristics.

Imager	UV NFOV IUN	UV WFOV IUW	Visible NFOV IVN	Visible WFOV IVW
Wavelength coverage (nm)	180–300	110–180	300–900	400–900
Field of view	1.6° × 1.3°	16° × 13°	1.6° × 1.3°	16° × 13°
Pixel size	108 × 91 μr	1.08 × 0.91mr	108 × 91 μr	1.08 × 0.91mr
Pixel resolution at 1000 km	100 m	1.0 km	100 m	1.0 km
Collecting area (cm^2)	130	25	130	25
Sensitivity (photons/cm^2·s·pixel)	0.08	1.30	0.10	0.78

Note: IUN = imager ultraviolet narrow; IUW = imager ultraviolet wide; IVN = imager visible narrow; IVW = imager visible wide; μr = microradians; mr = milliradians.

SIMULATION

Each of the four imagers produces a 256 × 244 pixel image that represents the total integrated photon count received during a sampling interval. The Laboratory's simulation was an attempt to model the measured effects as realistically as possible and to include sufficient flexibility to enable new data or tracked objects to be incorporated easily.

Simulated effects fall into four basic categories, and the features included under each are itemized as follows:

1. Target sets
   - Reentry vehicle (RV): cone shape
   - Reference object: sphere
   - Constant or variable surface reflectance
   - Rocket plumes
2. Terrestrial and planetary backgrounds
   - Rayleigh scattering
   - Airglow
   - Solar radiation
   - Moon and planets
3. Celestial backgrounds
   - Discrete stars
   - Diffuse stars
   - Zodiacal light
4. Instrumentation effects
   - Detection efficiency
   - Point spreading
   - Off-axis response
   - Poisson noise
   - AGC algorithms

For a given sampling interval, the photon count was assumed to be the sum of the contributions from each of the measured effects. Each of the four categories is discussed in the following paragraphs.

Target Sets

Target brightness depends on the target's size and shape, surface reflectivity, and distance from the sensor, as well as the orientation of the Sun relative to the target-sensor line-of-sight (LOS) vector. The orientation of nonspherical targets relative to the sensor and Sun vectors is also important. Two types of targets were modeled: a right circular cone and a sphere (see the boxed insert, Signals from Targets). Both were assumed to be point sources in the simulation. We assumed a perfectly diffuse reflecting surface and only considered the effects of solar reflected illumination. (These assumptions imply that the target radiance is the same in all directions.) A table of the Sun's power per unit area, $E(\lambda)$, at 1 AU (astronomical unit; 1 AU = the distance between the Sun and Earth, or 1.49×10^8 km) for wavelengths λ in the 120-930 nm band was used in all of the computations in this article. The units of $E(\lambda)$ are in photons/cm^2·s·nm.

To illustrate the sensitivity of the UVISI instruments, the expected measured photon count per second for a 100-cm-diam. sphere at a distance of 1000 km was computed for Sun angles varying from 0° to 175°. These results are shown in Fig. 1a for each of the four imagers. If β denotes the Sun angle, the measured effect is proportional to $\cos^2\beta/2$. It is also inversely proportional to the square of the range to the target and directly proportional to the square of the sphere's diameter. Figures 1b and 1c provide multiplicative scale factors to adjust for different target ranges and diameters, respectively. For example, the measured photon count per second for a 50-cm-diam. sphere will be 0.25 $[(50/100)^2]$ times smaller than that shown in Fig. 1a. This scale factor can be obtained from the curve shown in Fig. 1c for the diameter value of 50 cm. A similar procedure can be used to scale the measured values for different range distances.

The theory behind rocket plumes is very complex; their size, shape, and brightness levels are a complicated function of many parameters, not all well understood. It was beyond the scope of this simulation to try to incorporate a realistic model; however, some reasonable substitute was desired. To this end, Goldfinger (personal communication, 1989) developed an

SIGNALS FROM TARGETS

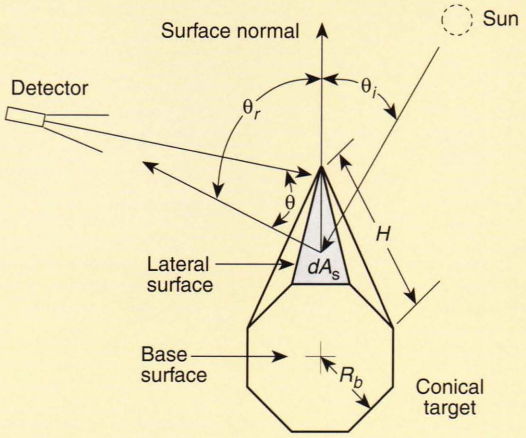

General target signature

$$C_{target} = \int_{\lambda} d\lambda \int_{A_s} \epsilon(\lambda)\alpha(\lambda)\frac{E_i(\lambda)\cos\theta_i A_d}{\pi r^2}\cos\theta_r \cos\theta \, dA_s$$

Conical target signature

$$C_{target} = \frac{A_d R_b^2 \cos\theta_i \cos\theta_r \cos\theta}{r^2}\int_{\lambda} \epsilon(\lambda)\alpha(\lambda)E_i(\lambda)d\lambda \quad \text{(base)}$$

$$+\frac{A_d R_b\sqrt{R_b^2+H^2}\cos\theta_i \cos\theta_r \cos\theta}{2\pi r^2}\int_{\phi_1}^{\phi_2} \cos\alpha_i \cos\alpha_r d\phi \int_{\lambda} \epsilon(\lambda)\alpha(\lambda)E_i(\lambda)d\lambda \quad \text{(lateral)}$$

where

A_d = detector aperture area,
θ_i = angle of incidence, relative to surface normal,
θ_r = angle of reflection, relative to surface normal,
θ = angle of target, relative to detector boresight,
α_i = angle of incidence, relative to basal coordinate system,
α_r = angle of reflection, relative to basal coordinate system,
ϕ = azimuth angle, basal coordinate system,
H = height of conical target,
R_b = base radius of target,
$\epsilon(\lambda)$ = instrument response curve,
$\alpha(\lambda)$ = reflectivity of target,
$E_i(\lambda)$ = irradiance of incident beam,
ϕ_1, ϕ_2 = range of angles observed from both Sun and detector,
dA_s = surface area increment,
θ = angle between detector boresight and line to increment,
r = range from target to detector, and
λ = wavelength.

empirical model with sufficient parameters to enable plumes of reasonable size and shape to be generated. From an analysis of rocket fuels,[7] approximate brightness levels were obtained and, together with the Goldfinger model, constitute the model implemented.

Terrestrial and Planetary Backgrounds

Rayleigh scattering is the reflection of solar radiation from molecules in the Earth's upper atmosphere. This effect is significant up to an altitude of 100 km above the Earth's surface. Some solar radiation is absorbed by these molecules and reemitted at different wavelengths, which can occur in many ways. Certain forms of this reemitted radiation are called airglow. Daytime and nighttime effects are dissimilar, and only the daytime (dayglow) contributions for altitudes below 300 km were included in the simulation. Rayleigh scattering and dayglow effects depend on existing atmospheric conditions, which vary with the 11.5-year solar flux cycle.

For a spaceborne imager, the integrated contribution of effects along the LOS of the instrument is recorded. Computational Physics, Inc. (CPI),[8] was contracted by APL to generate tables of these integrated intensities (for one set of atmospheric conditions) as a function of tangent altitude and solar zenith angle (SZA) for wavelengths in the ultraviolet and visible spectra.

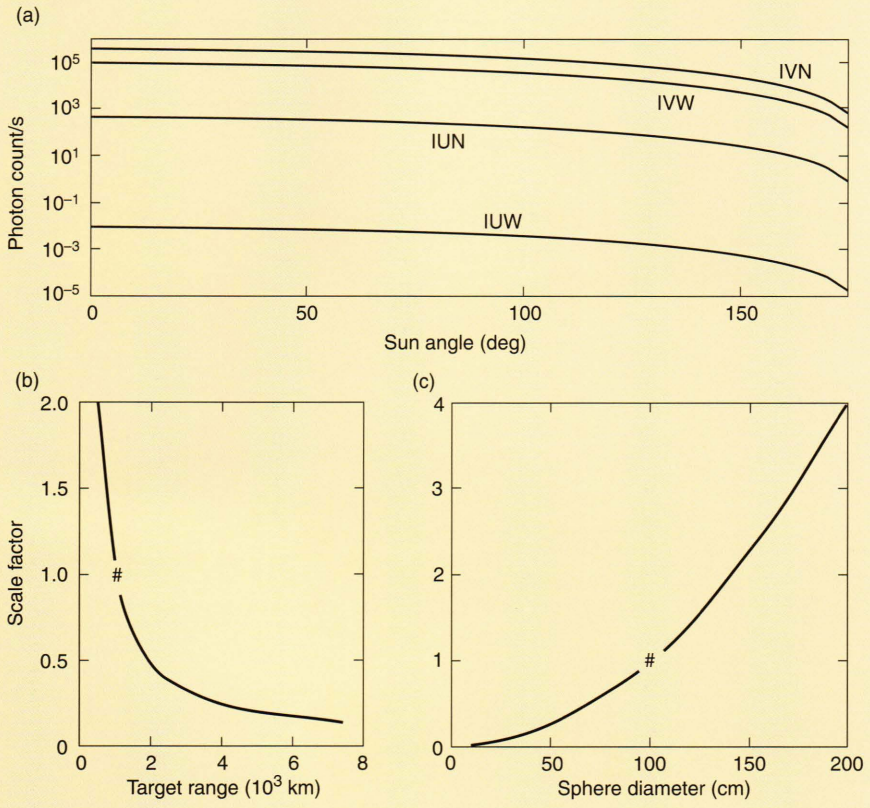

Figure 1. (a) Measured photon count per second versus Sun angle for a 100-cm-diam. sphere at a distance of 1000 km (IVN = imager visible narrow; IVW = imager visible wide; IUN = imager ultraviolet narrow; IUW = imager ultraviolet wide). (b) Scale factor for target range. (c) Scale factor for sphere diameter. The pound sign shown in (b) and (c) denotes values used in generating curves shown in (a).

Tangent altitude is the altitude relative to the Earth's surface at the perpendicular point of the LOS vector with an Earth radial vector. Negative altitudes imply that the LOS vector intersects the Earth's sphere. For positive values of tangent altitude, the SZA is the angle between the radius vector from the Earth's center through the tangent altitude point and the unit vector to the Sun. For negative values, the LOS intersection point with the Earth's surface is determined, and the Earth's radial vector through this point and the Sun's vector define the SZA.

Figures 2 and 3 show the computed dayglow and Rayleigh scattering contributions, respectively, for each of the four UVISI imagers for a select set of SZAs and tangent altitudes. As expected, the effects are greatest for a SZA of 0° and decrease with increasing angle. The Imager Ultraviolet Wide (IUW) is designed to be sensitive to wavelengths in the 110–180 nm band in which the Rayleigh scattering effects are nonexistent. Thus, these IUW curves are all zero, so they are not shown in Fig. 3. The calculations required to include Rayleigh scattering, dayglow, and other planetary effects in the FOV are presented in the boxed insert, Signals from Terrestrial and Planetary Backgrounds.

Celestial Backgrounds

The celestial background is composed of point source stars, faint diffuse stars, and zodiacal light. Each of these elements is handled in a different manner. (See the boxed insert, Signals from Celestial Backgrounds).

Some compromises had to be made in the simulation of background effects with regard to the star field. Even a modest-sized star catalog will contain several hundred thousand entries. Working with a catalog of this size would have a significant impact on both storage and computation time. The decision was made, for purposes of this simulation, to partition the stars into three different categories.

The first category consists of a set of about 5,000 bright stars, which was assembled by Daniell of CPI,[9,10] with visual magnitudes brighter than 6. These stars were treated as point sources. Galactic coordinates were available for this group along with information from which a reasonable estimate of star brightness as a function of wavelength could be computed.

The second category includes dim stars with visual magnitudes between 6 and 10. These were also treated as point sources but with randomly generated coordinates. For this group we used a table from Allen[11] that gives an estimate of the average brightness and distribution as a function of galactic latitude for each visual magnitude. We also ensured that the random stars for a given area of the sky are repeatable to preserve consistency between consecutive images generated in simulations of planned mission scenarios.

For point source stars, we also modeled motion smearing effects that may occur during the averaging time interval that an image is taken. We computed the number of pixels traversed during this time interval and then adjusted for motion in both brightness level and pixel position in the FOV. Stars being occulted by the Earth were eliminated. Figure 4 is a logarithmic plot showing the photon count per second that each of the four imagers would sense for stars with visual magnitudes ranging from −2.5 to 10.0.

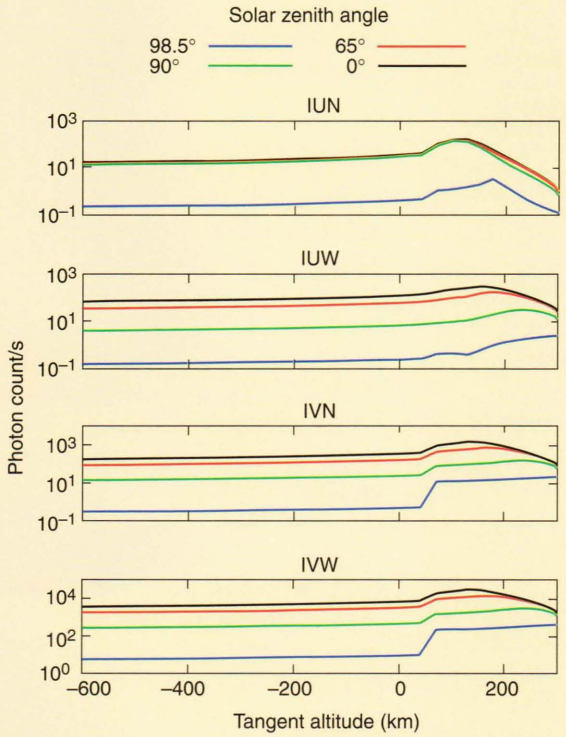

Figure 2. Computed dayglow contributions for each of the four UVISI imagers as a function of tangent altitude and solar zenith angle. (See Fig. 1 caption for imager definitions.)

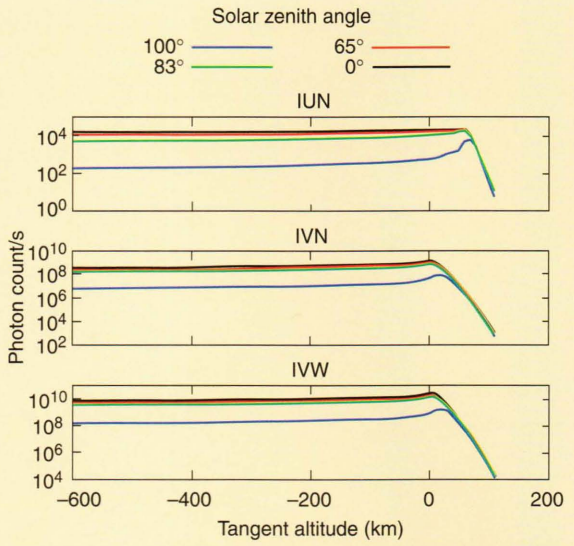

Figure 3. Computed Rayleigh scattering contributions for three of the four UVISI imagers as a function of tangent altitude and solar zenith angle. The IUW curves are not shown because they were all zero. (See Fig. 1 caption for imager definitions.)

The last group consists of dim stars with visual magnitudes dimmer than 10. These were treated as diffuse sources. A table giving the average brightness of all dim stars in this group as a function of galactic latitude was used to compute a background brightness throughout the entire FOV.

Zodiacal light is sunlight scattered by interplanetary dust. The brightness levels are constant only in a reference system in which the Sun is stationary. Daniell[12] generated a table of brightness values as a function of ecliptic latitude and elongation. Elongation is the difference between the ecliptic longitude of the point being observed and the ecliptic longitude of the Sun. The brightness levels are in units of brightness of a star of visual magnitude 10 at 550 nm. Values are given for every 5° in latitude (0°–90°) and 5° in elongation (0°–180°). These entries are converted to photons/cm^2·s·sr·nm by a multiplicative scale factor of 3377. Daniell[12] also provided a table of the normalized (at 550 nm) spectral distribution of zodiacal light covering the wavelength band of 120–897 nm. With this information, the contribution at the pixel level from zodiacal light can be computed. Figure 5 is a

SIGNALS FROM TERRESTRIAL AND PLANETARY BACKGROUNDS

$$C_{\text{terrestrial}} = A_d A_{pl}\left(\frac{\pi R_{pl}^2}{R_{epl}^2}\right)\left(\frac{R_{se}^2}{R_{spl}^2}\right)\int_\lambda \epsilon(\lambda) E_s(\lambda)\, d\lambda \quad \text{(planets)}$$

$$+ A_d A_m\left(\frac{\pi R_m^2}{R_{em}^2}\right)\left(\frac{R_{se}^2}{R_{sm}^2}\right)\int_\lambda \epsilon(\lambda) E_s(\lambda)\, d\lambda \quad \text{(Moon)}$$

$$+ A_d \Omega_p \int_\lambda \epsilon(\lambda)[F_D(\lambda, a_t, \alpha_s) + F_R(\lambda, a_t, \alpha_s)]\, d\lambda \quad \text{(Earth limb)},$$

where

A_{pl}, A_m = planet, Moon albedo,
R_{pl}, R_m = planet, Moon radius,
R_{epl}, R_{em}, R_{se} = range from Earth to planet, Earth to Moon, Sun to Earth,
R_{spl}, R_{sm} = range from Sun to planet, Sun to Moon,
$E_s(\lambda)$ = solar irradiance at Earth orbit,
$F_D(\lambda, a_t, \alpha_s)$ = dayglow radiance,
$F_R(\lambda, a_t, \alpha_s)$ = Rayleigh scattered radiance,
a_t, α_s = tangent altitude, solar zenith angle,
Ω_p = pixel solid angle of detector, and
A_d = aperture area of detector.

In sum, $x \geq -R_p \cos\theta$, $x^2 + y^2 \leq R_p^2$, where θ is the angle between sensor–Moon vector and Sun–Moon vector, R_p is Moon radius in pixels, and λ is wavelength.

SIGNALS FROM CELESTIAL BACKGROUNDS

$$C_{\text{celestial}} = A_d \sum_m \left[A_m^{UV} \int_{120}^{365} \frac{\epsilon(\lambda)\,d\lambda}{\lambda^4 \left(e^{hc/\lambda k T_{mU}} - 1\right)} + A_m^{VIS} \int_{365}^{650} \frac{\epsilon(\lambda)\,d\lambda}{\lambda^4 \left(e^{hc/\lambda k T_{mV}} - 1\right)} + A_m^{IR} \int_{650}^{1000} \frac{\epsilon(\lambda)\,d\lambda}{\lambda^4 \left(e^{hc/\lambda k T_{mI}} - 1\right)} \right]$$

$$+ A_d \sum_j A_j^G(\alpha,\delta) \int_\lambda \epsilon(\lambda) G(\lambda)\,d\lambda \quad \text{(weak discrete stars)}$$

$$+ A_d \Omega_p A_D(\alpha,\delta) \int_\lambda \epsilon(\lambda) G(\lambda)\,d\lambda \quad \text{(weak diffuse stars)}$$

$$+ 3377 A_d \Omega_p A_Z(\psi,\xi) \int_\lambda \epsilon(\lambda) S(\lambda)\,d\lambda \quad \text{(zodiacal light)},$$

where

T_{mU}, T_{mV}, T_{mI} = effective temperature for bright, discrete stars, $0 < m < 6$ (computed),
A_m^{UV}, A_m^{VIS}, A_m^{IR} = effective amplitude for bright, discrete stars, $0 < m < 6$ (computed),
$A_j^G(\alpha, \delta)$ = coefficients for weak, discrete stars, $6 < m < 10$ (tabulated, randomized),
$G(\lambda) = -0.459 + 4.18 \times 10^{-3}\,\lambda - 2.79 \times 10^{-6}\,\lambda^2$,
$S(\lambda)$ = normalized solar spectrum
$A_D(\alpha, \delta)$ = diffuse star distribution (tabulated),
$A_Z(\psi, \xi)$ = zodiacal light distribution (tabulated),
(α, δ) = right ascension, declination,
(ψ, ξ) = elongation and latitude,
h = Planck's constant,
c = speed of light,
k = Boltzmann's constant, and
A_d = aperture area of detector.

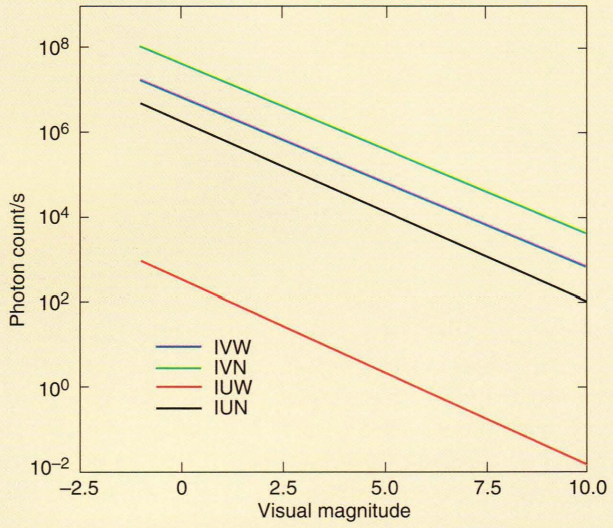

Figure 4. Star brightness levels as a function of visual magnitude, as sensed by each of the imagers. (See Fig. 1 caption for imager definitions.).

logarithmic plot of the zodiacal light contributions at the pixel level for each of the four imagers. The photon count per second is given as a function of ecliptic latitude for seven different elongation values.

Instrumentation Effects

For instrumentation effects, an attempt is being made to model characteristics of the UVISI instruments (see the boxed insert, Signals from Instrumentation Effects). The photon detection efficiencies[13,14] for each of the four imagers as a function of wavelength are shown in Fig. 6. They define the conversion from photons sensed to counts recorded by the instrument. Peak efficiency occurs near the center of the wavelength band of each instrument.

Darlington[15] has defined a point spread function to describe the telescope, image intensifier, and charged-coupled device effects on the image obtained (i.e., because of their characteristics, a ray of incoming light is distributed over several pixels surrounding the center beam point, and the point spread function defines how this distribution occurs). Each of the instruments is designed to exclude all but directly entering rays of light. For a given design, point source transmittance (PST) values can be computed to express the degree to which indirect light is excluded. The PST values have been tabulated by Harris[16,17] to reflect the off-axis rejection capabilities of the optical and baffle geometries most likely to be used. PST values are expressed as a function of the look angle relative to the LOS vector for both the narrow and wide FOVs (see Fig. 7). These values are defined as the ratio of irradiance at the input aperture (baffle opening) to the irradiance at the detector (intensifier).

In the simulation, we compute the off-axis rejection effects for the center pixel and then assume (as a first order approximation) that it would be the same for all pixels in the FOV. In theory, the point spread function and off-axis effects should be convolved; however, in the simulation they are treated as additive. The major contributors to off-axis effects are Rayleigh scattering

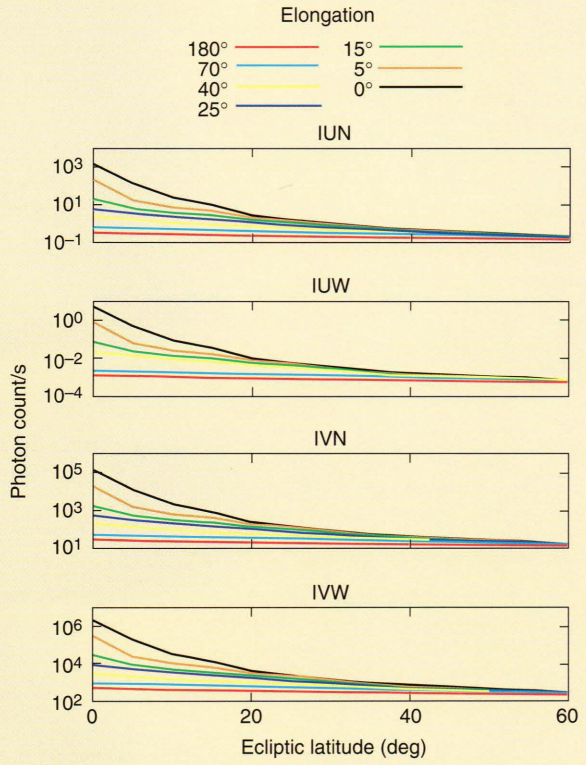

Figure 5. Zodiacal light effects as a function of ecliptic latitude and elongation. (See Fig. 1 caption for imager definitions.)

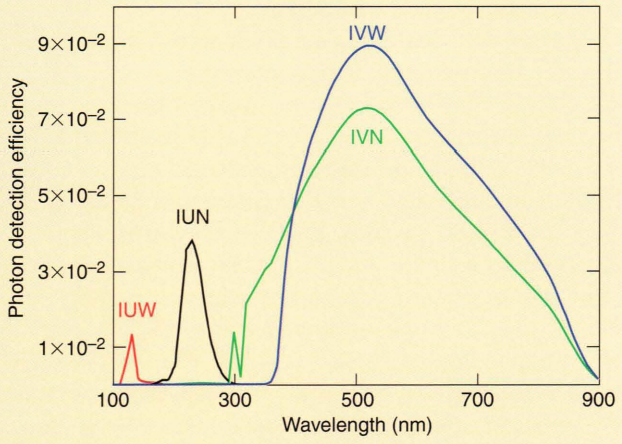

Figure 6. Photon detection efficiencies (optical + quantum) for the four UVISI imagers. (See Fig. 1 caption for imager definitions.)

SIGNALS FROM INSTRUMENTATION EFFECTS

Point spreading

$$C_{PSF}(X,Y)=\frac{C_{pt}}{2\pi\sigma^2}\int_{X-dx}^{X+dx}du\int_{Y-dy}^{Y+dy}\exp(-r^2/2\sigma^2)dv,$$

where C_{pt} is the unadjusted count from a point source and

$$r^2=(u-X_1)^2+(v-Y_1)^2,$$

$$\sigma=\left[1+\frac{(X_1-W)^2dx^2+(Y_1-W)^2dy^2}{W^2(dx^2+dy^2)}\right]\frac{dx}{2.354},$$

dx = half-width pixel size in x,
dy = half-width pixel size in y,
W = half the number of pixels in x,
(X_1, Y_1) = position of point source in image plane coordinates, and
(X, Y) = position of pixel in image plane coordinates.

Off-axis rejection

$$C_{\text{off-axis}}=\int_0^{2\pi}d\phi\int_0^{\pi/2}\sin\theta\,PST(\theta,\phi)C_{\text{terrestrial}}(\theta,\phi)d\theta,$$

where $C_{\text{terrestrial}}$ is the unadjusted count rate from lunar, solar, and Earth-limb radiation and

$PST(\theta, \phi)$ = point source transmittance function (normalized),
θ = elevation angle relative to boresight, and
ϕ = azimuth angle relative to boresight.

Note: (θ, ϕ) coordinates are equivalent to (X, Y) pixel coordinates of the image plane (see above).

and dayglow. Figure 8 shows the magnitude of off-axis effects for each of the imagers as a function of tangent altitude for four different SZAs.[18]

The application of Poisson noise was an attempt to model the quantum effects of light propagation. This noise was added at the pixel level after all the simulated effects had been integrated into the image. Poisson noise contributions are most noticeable on the weaker signals being measured by the instruments such as faint stars and zodiacal light.

Automatic gain control algorithms developed by Carbery[6] provide a means for adjusting the sensors for scene brightness. The dynamic count range for each pixel is 0 to 4095. For a given scene, Carbery's algorithm attempts, via gain settings, to maintain the pixel count well inside this count span. Gain values are constantly adjusted on the basis of the distribution of counts obtained on the previously processed image. The simulation was able to test the effectiveness of these algorithms.

RESULTS

As is shown in Figs. 1 through 5 and 8, the dynamic range of the modeled signals is quite large. Therefore, the presence of a bright star or a strong Rayleigh scattering signal in the FOV will preclude the observance of weaker signals, such as faint stars and/or zodiacal light. However, to illustrate the contributions of the modeled signals in the images, image enhancement techniques and pseudocolor were applied to increase the dynamic range observable in a given image. Poisson

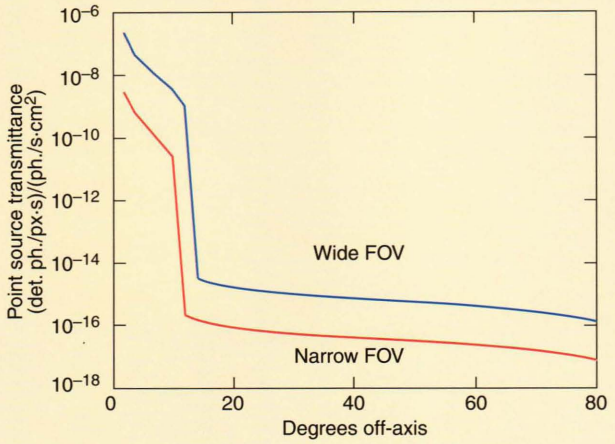

Figure 7. Point source transmittance (PST) function for single point source at center of view. The PST is given in terms of detected photons per pixel per sample time (frame time) divided by the incident irradiance.

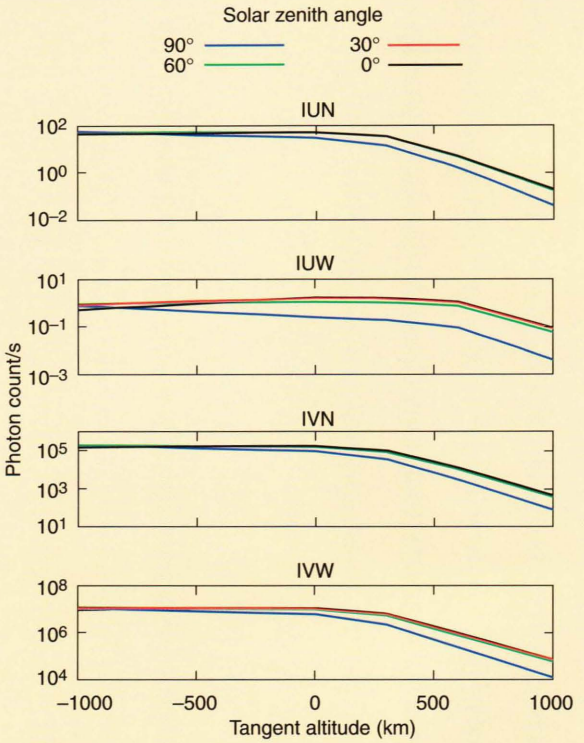

Figure 8. Off-axis contributions for the four UVISI imagers as a function of tangent altitude for four solar zenith angles. (See Fig. 1 caption for imager definitions.)

noise effects were not included, since they tend to hide the presence of the lower-amplitude signals (faint and diffuse stars and zodiacal light).

Figure 9 presents simulated images of the same area of the sky as seen by each of the four UVISI instruments. The modeled rocket plume appears in the center of three of the images (Figs. 9a,c,d). Its signal was too weak to be seen by the IUW instrument (Fig. 9b). Rayleigh scattering, dayglow, and off-axis contributions appear at the bottom of the wide FOV instruments (Figs. 9b and 9d), but were not within the angular range of the narrow-field imagers. Rayleigh scattering and dayglow effects are evaluated on a dense, uniformly spaced grid covering the FOV and then linearly interpolated for the remaining pixels.

Diffuse stars and zodiacal light contributions are also computed on a uniformly spaced grid. A quadratic surface over the FOV is fitted to these points and then used to provide values at the pixel level. This effect is manifested by background shading variations. They are apparent only in the visible wide view (Fig. 9d).

Point source stars are also visible in each of the four images. The smearing effects due to spacecraft attitude motion are more noticeable in the narrow-field images (Figs. 9a and 9c).

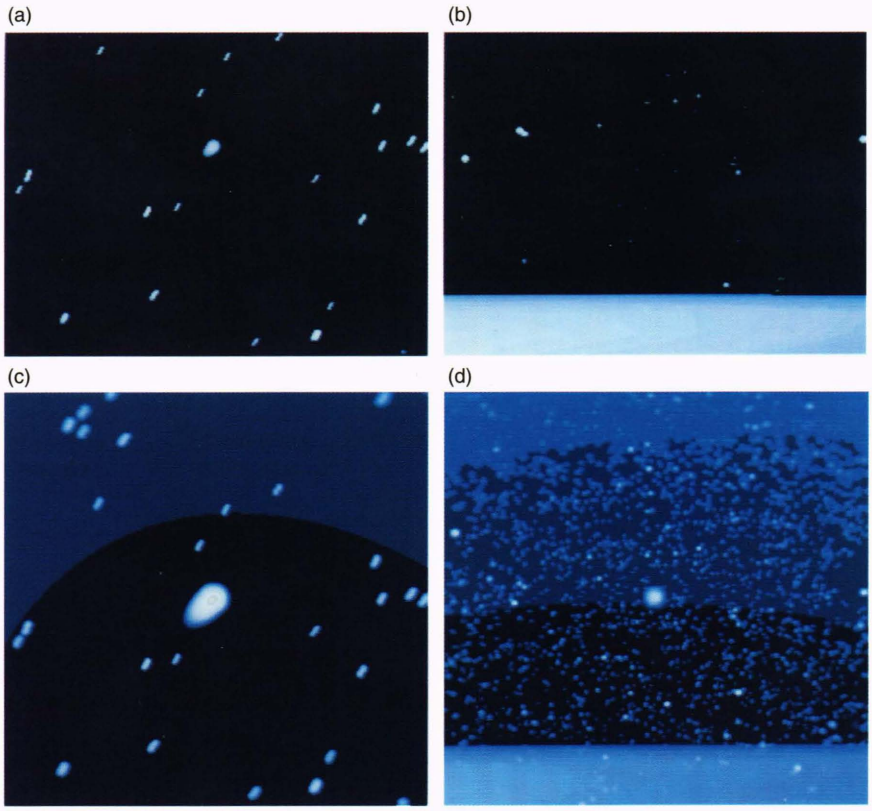

Figure 9. Spacecraft view as seen by each of the four UVISI imagers: (a) imager ultraviolet narrow (IUN), (b) imager ultraviolet wide (IUW), (c) imager visible narrow (IVN), (d) imager visible wide (IVW).

This software program has been used in simulations of many of the experiments planned for the MSX mission and in tests of onboard programs. It also has served as a valuable tool in assessing the capabilities of the UVISI instruments. After the MSX is launched and real images are obtained, this simulation can also be used to test the theoretical models that generated the data files incorporated in the software program.

REFERENCES

1 Yionoulis, S. M., *Imager: UVISI Scene Generator*, JHU/APL S1A-025-90 (15 Mar 1990).
2 Yionoulis, S. M., *SPIMS: UVISI Spectrographic Image Simulation*, JHU/APL S1A-023-91 (20 Mar 1991).
3 Heyler, G. A., and Murphy, P. K., "Midcourse Space Experiment (MSX) Closed-Loop Image and Track Processing," in *Proc. SPIE OE/Aeros. Sens. Conf.* (4-8 Apr 1994), Orlando, FL (in press).
4 Waddell, R. L., Jr., Murphy, P. K., and Heyler, G. A., "Image and Track Processing in Space, Part I," in *Proc. AIAA Comput. Aeros. 9 Conf.* (19-21 Oct 1993), pp. 576-585.
5 Murphy, G. K., Heyler, G. A., and Waddell, R. L., Jr., "Image and Track Processing in Space (Part II)," in *Proc. AIAA Comput. Aeros. 9 Conf.* (19-21 Oct 1993), pp. 586-596.
6 Carbary, J. F., and Hook, B. J., *UVISI Gain Control*, JHU/APL S1G-044-92 (31 Mar 1992).
7 Bement, D., Mule, J., Adelmann, P., Kumar, K., McLure, M., et al., *Special Projects Flight Experiment Independent Mission Planning Evaluation*, APL Special Rpt. prepared for Strategic Defense Initiative Organization, Brilliant Pebbles Task Force, The Pentagon (19 Oct 1992).
8 Strickland, D. J., Duval, P. D., and Daniell, R. E., *Terrestrial Diffuse Sources in the Visible and UV*, Computational Physics, Inc. (Apr 1987).
9 Daniell, R. E., *Description of Database of Stars Brighter than 6th Magnitude*, Computational Physics, Inc. (6 Mar 1986).
10 Daniell, R. E., *Algorithm for Estimating the Spectrum of a Star from Its Spectral Class and Visual Magnitude*, Computational Physics, Inc. (13 Mar 1987; Rev 13 July 1989).
11 Allen, C. W., *Astrophysical Quantities*, Athlone, London, p. 244 (1973).
12 Daniell, R. E., *Extraterrestrial Diffuse Sources in the Visible and Ultraviolet*, Computational Physics, Inc. (11 Jun 1987).
13 Carbary, J. F., *Sensitivities of the Nine UVISI Sensors*, JHU/APL S1G-055-1992 (16 Apr 1992).
14 Carbary, J. F., *Errors Estimates for Sensitivities of the Nine UVISI Sensors*, JHU/APL S1G-065-1992 (16 May 1992).
15 Darlington, E. H., *Point Spread Function for Sensor Simulation*, JHU/APL S1I-1-267 (16 Mar 1989).
16 Harris, T. J., *Preliminary Estimates of Stray Light for the UVISI Imagers*, JHU/APL F1F(2)89-U-038 (6 Feb 1989).
17 Harris, T. J., *Tabulated Point Source Transmittance Values*, JHU/APL F1F(2)89-U-294 (5 Oct 1989).
18 Yionoulis, S. M., *UVISI Dayglow, Rayleigh Scattering Off-axis Effects*, JHU/APL S1A-106-90 (13 Dec 1990).

ACKNOWLEDGMENTS: This simulation was made possible by the contributions of many people. The tables and formulas provided by Computational Physics, Inc., and Rob Daniell were a major contribution. Jim Kraiman of Dynamics Technology, Inc., Edward H. Darlington, Steve Hansen, and Glen H. Fountain also played an important role in determining how each of the various effects should be implemented. Terry J. Harris provided the point source transmittance values used in modeling off-axis effects, and Andrew D. Goldfinger derived the plume model used in the simulation. James F. Carbary generated revised instrument detection efficiencies and developed the AGC algorithms.

THE AUTHOR

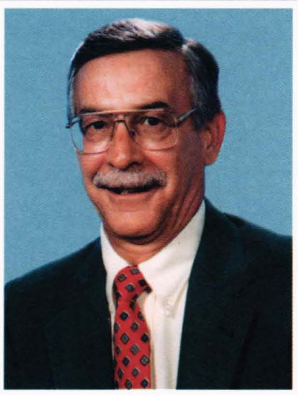

STEVE M. YIONOULIS received his B.S. and M.S. degrees in applied mathematics from North Carolina State University, Raleigh, in 1959 and 1961, respectively. He joined the Space Department of APL in 1961 and is a member of the Principal Professional Staff. His areas of professional interest include satellite orbital mechanics, satellite geodesy, and upper atmospheric density modeling. Mr. Yionoulis has also been engaged in image processing for medical programs and in the application of neural networks for pattern recognition. His current interests are in interplanetary mission analysis.